semiconductors and heterogeneous integration

MDPI

Article

Critical Switching Current in Perpendicular SOT-MRAM Devices

Bernhard Pruckner *, Viktor Sverdlov and Siegfried Selberherr

Institute for Microelectronics, TU Wien, Gußhausstraße 27-29/E360, 1040 Vienna, Austria; sverdlov@iue.tuwien.ac.at (V.S.); selberherr@tuwien.ac.at (S.S.)

* Correspondence: pruckner@iue.tuwien.ac.at

Abstract

We investigate the magnetization reversal of a ferromagnetic layer by an applied in-plane charge current in SOT-MRAM devices utilizing the spin Hall effect (SHE) as well as the SHE and an applied in-plane external magnetic field. We also consider the case of a strong field-like torque generated by other SOT mechanisms, such as Rashba-type interface effects. By deriving the steady-state solutions of the driven system and evaluating their stability, we identify two distinct mechanisms that govern deterministic switching. In the first-oscillation-driven mechanism, the magnetization is pushed past an unstable steady-state by the initial deviation following the current onset, after which it relaxes towards an alternative steady-state branch in the opposite hemisphere. As lower damping produces a larger initial oscillation amplitude at a given current, the critical current depends on the Gilbert damping constant α. We show that the usual damping-independent critical current expression is recovered in the overdamped regime with $\alpha \geq 1$. In the instability-driven mechanism, activated by field-like torque, even a small initial oscillation grows until the equator is crossed and the magnetization ends in the opposite hemisphere. The critical switching current is the minimum of both mechanisms. Thus, the steady-state landscape reveals distinct current regimes, identifying optimal operating regimes for perpendicular reversal.

Keywords: macrospin; SOT MRAM; deterministic perpendicular switching; Landau–Lifshitz–Gilbert equation

1. Introduction

Magnetoresistive random access memory (MRAM) is a non-volatile memory offering high endurance, nanosecond switching, and long retention, and promises to overcome the limitations of conventional CMOS-based memories in automotive systems, Internet-of-Things devices, and AI accelerators [1,2]. STT-MRAM is available in 16 nm FinFET technology [3], and an 8 nm perspective for automotive applications has been demonstrated [4,5], but its reliability at high speed remains a critical concern [6].

Spin-orbit torque (SOT)–MRAM is a leading candidate for next-generation non-volatile magnetoresistive memory offering high endurance and sub-nanosecond switching. It is considered for use in cache memory, Internet-of-Things applications, and automotive equipment, where power efficiency and reliability are critical [7]. A typical SOT-MRAM cell is shown in Figure 1. Like in STT-MRAM, the information is encoded in the relative orientation of perpendicularly magnetized ferromagnetic layers separated by a tunnel barrier, forming a magnetic tunnel junction (MTJ). The magnetization orientation of the top reference layer (RL) is fixed, while that of the lower free layer (FL) can be manipulated. The resistance of the MTJ depends on the relative orientation of its layers. This information is read by running a small read current through the MTJ and measuring its resistance.

Check for updates

Academic Editor: Lining Zhang

Received: 8 July 2026
Revised: 26 August 2026
Accepted: 10 September 2026
Published: 15 September 2026

Copyright: © 2026 by the authors. Licensee MDPI, Basel, Switzerland. This article is an open access article distributed under the terms and conditions of the Creative Commons Attribution (CC BY) license.

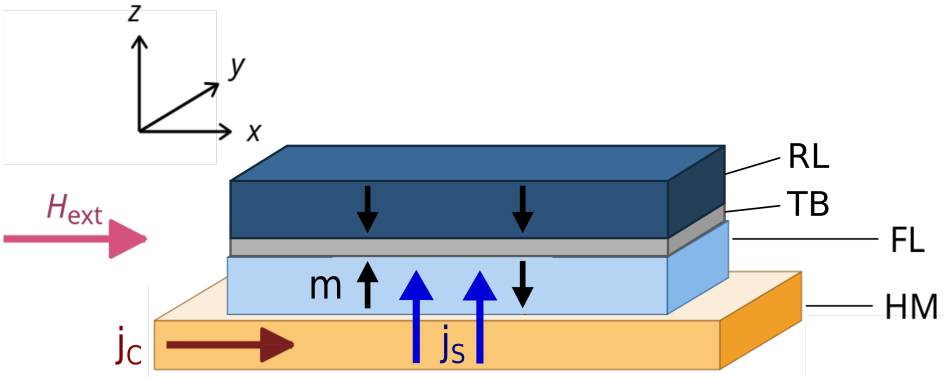


Figure 1. Schematic of the SOT device. An MTJ, a stack of a ferromagnetic reference layer (RL)/tunnel barrier (TB)/ferromagnetic free layer (FL) with a perpendicular magnetic anisotropy on top of a heavy metal (HM) SOT write layer. The magnetization **m** is indicated by black arrows. The charge current j_C (indicated by the dark red arrow) flows along $\hat{\mathbf{x}}$ through the HM. The spin Hall effect (SHE) generates spin current $\mathbf{j_s}$ polarized along $-\hat{\mathbf{y}}$ (indicated by blue arrows) that impinges into the FL. An optional external magnetic field $\mathbf{H}_{\text{ext}}$ (indicated by the pink arrow) may be applied along $\hat{\mathbf{x}}$ to facilitate deterministic perpendicular switching.

In contrast to STT-MRAM, the large write current does not run through the MTJ. It is applied through a SOT-generating stack. The main element of the spin-orbit stack is a heavy metal (HM) layer, typically W, Ta, or Pt. A charge current j_C along $\hat{\mathbf{x}}$ generates a spin current with polarization σ in the HM via the spin Hall effect (SHE) [8,9], which impinges into the FL. The SOT then acts on the magnetization of the FL, making it flip. SOT has emerged as an attractive writing mechanism: it decouples read and write current paths and enables intrinsically fast switching [10–13].

SOT-MRAM is a three-terminal device. To reduce the cell footprint and to minimize the influence of external magnetic fields, perpendicular (p)-MTJs are required, which use magnetic materials with a high perpendicular magnetic anisotropy (PMA). Thin layers of CoFeB grown on MgO are commonly used to fabricate p-MTJs as they develop a strong interface-induced PMA [14]. To achieve the deterministic switching of the perpendicular FL, an in-plane external magnetic field $\mathbf{H}_{\text{ext}}$ along the current direction is required [15].

Commercialization of SOT-MRAM demands material and structural optimizations of SOT-MRAM cells to minimize the energy at fast switching. A central design quantity is the critical current density j_{crit} required to reverse the FL magnetization. It determines the minimum threshold current. Within a macrospin Landau–Lifshitz–Gilbert (LLG) framework, an analytic expression for the switching current density for highly damped systems

$$j_{\text{crit}} = \frac{2e\,M_S d_f}{\hbar\,\theta_{\text{SHE}}}\left(\frac{H_K^{\text{eff}}}{2} - \frac{H_x}{\sqrt{2}}\right), \tag{1}$$

was presented [16]. It was obtained based on the assumption that the magnetization, initially along $+\hat{\mathbf{z}}$, is pushed in-plane by the SOT, parallel to the spin current polarization σ, while the external field $\mathbf{H}_{\text{ext}}$ slightly shifts the magnetization into the lower hemisphere of $m_z < 0$, so that after the current is turned off, the magnetization relaxes towards $-\hat{\mathbf{z}}$.

However, as has been demonstrated in [17], expression (1) overestimates the switching current relative to experiments and micromagnetic simulations. It was argued that the appearance of a plateau with $m_y \approx 0$, accompanied by the reversal of the magnetization precession chirality, is important for deterministic switching. The determined critical current is indeed lower than that predicted by (1). Similar to (1) the analysis in [17] was based on the stationary LLG equation and the analytical solution is damping-independent.

Taniguchi et al. [18] showed that, in the presence of field-like torque of a relative strength β, the critical current becomes small at weak Gilbert damping. As the critical current j_{crit} is predicted to scale as $j_{\mathrm{crit}} \propto \sqrt{\alpha/(-\beta)}$ if $\alpha \ll |\beta|$ (with $\beta < 0$ in the beneficial regime), field-like torque appears to be beneficial for reducing the switching energy. The case of a nonzero field-like torque was also investigated in [17], with the conclusion that the critical current develops a shallow maximum at not very large β and is damping-independent. This seems to contradict the findings in [18] and requires clarification.

In this work, we present a unified approach, which recovers the existing models as special cases. It is built on two ingredients: the steady-state landscape of the driven system and the system's dynamical behavior with respect to the steady-state landscape following the current onset. It is found that deterministic switching proceeds through one of two mechanisms. In the first-oscillation-driven mechanism, the first oscillation of m_z, after current onset, crosses an unstable steady-state branch, which forces the magnetization to relax to the steady-state solution in the opposite hemisphere, resulting in magnetization reversal after the current is off. The plateau [17] on the trajectory is due to magnetization dynamics slowing down before overcoming the unstable steady state. Since the trajectory dynamics, and in particular the amplitude of the first deviation of the magnetization from its initial state, depend on damping, the critical current depends on α. At weaker damping, the first oscillation amplitudes are larger, which helps to overcome the unstable steady state at lower currents. We also determine that the expression (1) is recovered in the overdamped regime $\alpha \geq 1$.

In the instability-driven mechanism, the field-like torque with negative β, typical for W/CoFeB, Ta/CoFeB, and Pt/Co [19], completely alters the steady-state landscape by destabilizing some solutions, which are stable at $\beta = 0$. In this case, even a small initial deviation grows into increasing oscillations, so that the trajectory eventually crosses into the opposite hemisphere and switching occurs. A sufficiently large negative β activates the instability-driven mechanism, yielding a reduced critical current with the scaling $j_{\mathrm{crit}} \propto \sqrt{\alpha/(-\beta)}$; $\beta < 0$ predicted in [18].

The paper is organized as follows. Section 2 introduces and verifies the model. It also highlights one of our central results: a clear dependence of the critical switching current density on damping α. The dependence on α is explained within the steady-state framework developed in Section 3 and the first-oscillation-driven switching mechanism introduced in Section 4, which highlights the pivotal roles of the initial magnetization dynamics and damping. The field-like torque is introduced in Section 5. Based on the steady-state framework, the instability-driven switching mechanism is determined, which is characteristic of the presence of the field-like torque of a particular sign [18]. This mechanism significantly reduces the switching current density at low damping. Section 6 discusses the relation of the model to experiments. Section 7 summarizes our findings.

2. Model

We analyze the FL switching behavior in the HM/FL bilayer of Figure 1. The normalized magnetization $\mathbf{m}$ of the free layer obeys the Landau–Lifshitz–Gilbert–Slonczewski (LLGS) equation:

$$\begin{aligned}\frac{\partial \mathbf{m}}{\partial t} = &-\gamma\, \mathbf{m} \times \mathbf{H}_{\mathrm{eff}} + \alpha\, \mathbf{m} \times \frac{\partial \mathbf{m}}{\partial t} \\ &- \gamma B_{\mathrm{SOT}}\, \mathbf{m} \times (\mathbf{m} \times \boldsymbol{\sigma}) - \gamma\beta B_{\mathrm{SOT}}\, \mathbf{m} \times \boldsymbol{\sigma},\end{aligned} \tag{2}$$

where γ is the gyromagnetic ratio, α is the Gilbert damping constant, and β is the ratio of field-like to damping-like torque. The first term describes a precession of $\mathbf{m}$ around $\mathbf{H}_{\mathrm{eff}}$. The second term is the Gilbert damping of $\mathbf{m}$ toward $\mathbf{H}_{\mathrm{eff}}$. The third term is the

damping-like SOT $\boldsymbol{\tau}_{\mathrm{DL}}$ pushing $\mathbf{m}$ towards the direction of spin-polarization $\boldsymbol{\sigma}$. The fourth term is the field-like SOT $\boldsymbol{\tau}_{\mathrm{FL}}$, pointing normal to $\mathbf{m}$ and $\boldsymbol{\tau}_{\mathrm{DL}}$. Both torque terms arise from the spin current injected into the free layer.

In a macrospin description every mechanism producing a field-like torque $\mathbf{m} \times \boldsymbol{\sigma}$ is indistinguishable from any other; thus, the FLT term includes contributions from the bulk spin Hall torque, the interfacial spin Rashba–Edelstein contribution [20], and the orbital contributions of the orbital Hall and orbital Rashba–Edelstein effects [21]. Since these contributions originate largely at the interfaces, β is an effective phenomenological parameter characteristic of a complete stack rather than a material [19,21].

The torque model used in Equation (2) does not include higher-order angular dependence contributions. As it is experimentally demonstrated in [19], additional contributions are negligible for common Co/Pt and Ta/CoFeB stacks, where (2) describes the magnetization dynamics adequately.

The spin current polarization is $\boldsymbol{\sigma} = \mp\hat{\mathbf{y}}$ for a positive or negative spin Hall angle, respectively. The effective field includes the effective uniaxial anisotropy field along $\hat{\mathbf{z}}$ with strength H_K and the applied external field along $\hat{\mathbf{x}}$ with strength H_x.

$$\mathbf{H}_{\mathrm{eff}} = H_K m_z \, \hat{\mathbf{z}} + H_x \, \hat{\mathbf{x}} \tag{3}$$

Here, the demagnetizing field of the thin-disc geometry [22] is absorbed into the effective anisotropy $H_K = H_k - N_d M_S$, where N_d is the demagnetization factor along $\hat{\mathbf{z}}$ and M_S is the saturation magnetization. The damping-like SOT amplitude is

$$B_{\mathrm{SOT}} = \frac{\hbar \, |\theta_{\mathrm{SHE}}|}{2e \, M_S d_f} \, j_C, \tag{4}$$

where $\hbar$ is the reduced Planck constant, e is the elementary charge, θ_{SHE} is the spin Hall angle of the heavy-metal layer, d_f is the free-layer thickness, and j_C is the charge current density. Equation (2) is integrated numerically using a fourth-order Runge–Kutta scheme with a fixed time step of 2×10^{-13} s. The initial magnetization is set to $\mathbf{m}_0 = \hat{\mathbf{z}}$.

For a threshold-driven mechanism, the switching current depends on the pulse duration. To determine the lowest switching threshold current in simulations, switching is evaluated with a rectangular current pulse of duration $t_{\mathrm{p}} = 10$ ns for the first-oscillation-driven mechanism and $t_{\mathrm{p}} = 100$ ns for the instability-driven mechanism. The a sufficiently long pulse length is chosen to settle the magnetization into a stable steady state. The critical current j_{crit} is the smallest current for which switching occurs, determined on a sweep of granularity $\Delta j_C = 10^9$ A/m^2.

To refine the determination of j_{crit} for the instability-driven mechanism, the growth rate of the oscillations is additionally investigated. We evaluate the rate by determining whether $m_{z|first} - m_{z|last} < 0$ within the applied current pulse windows, with $m_{z|first}$ and $m_{z|last}$ being the m_z-amplitude of the first and last oscillation within the current pulse, respectively. This condition indicates that the stable branch has become unstable and the trajectory eventually leaves it to converge toward a neighboring stable state.

To validate our approach, we adopt the material parameters from [17]: effective anisotropy $H_K = 0.091$ T, saturation magnetization $M_S = 1.3$ T, free-layer thickness $d_f = 1.2$ nm, and spin Hall angle $\theta_{\mathrm{SHE}} = 0.03$, unless specified otherwise.

Using these parameters from [17] and the damping-like torque only ($\beta = 0$), we reproduce the switching behavior shown in Figure 2a at the reported critical current $j_{\mathrm{crit}} = 2.604 \times 10^{12}$ A/m^2, for Gilbert damping $\alpha = 0.02$. However, increasing the damping to $\alpha = 0.03$ already suppresses switching (Figure 2b), demonstrating that the threshold current clearly depends on α. Reducing the external field to $H_x = 5$ mT increases the

critical current by roughly 60% (from 2.604 to 4.143×10^{12} A/m^2) for $\alpha = 0.02$ (Figure 3a). Even though the dynamics look different, the trajectory displays a characteristic plateau $m_y \approx 0$ followed by the reversal of precession chirality before the magnetization proceeds into the low hemisphere and relaxes to the switched state $m_z = -1$ after the current is off, in agreement with [17]. However, as before, a slight increase in the damping constant to $\alpha = 0.03$ prevents switching (see Figure 3b). The magnetization remains in the upper hemisphere and relaxes back to its initial state when the current is switched off. Numerical simulations clearly demonstrate that the critical current depends not only on damping but also on the external field.

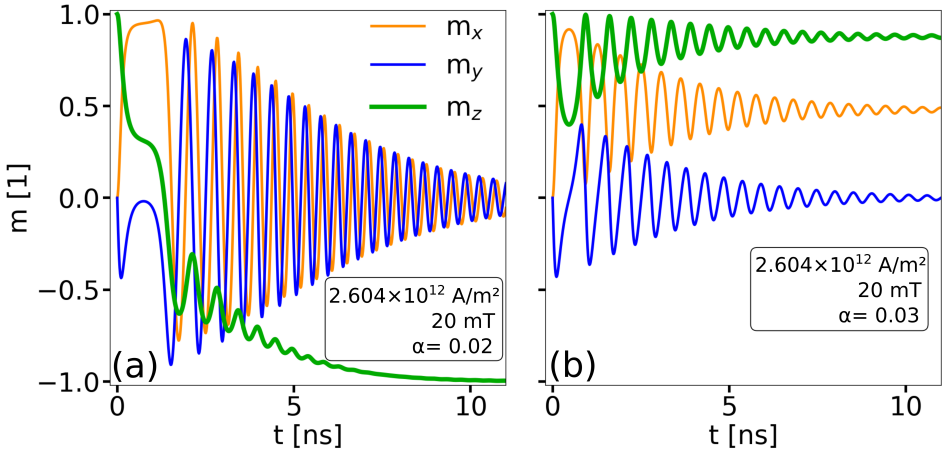


Figure 2. Time evolution of the magnetization of the system depicted in Figure 1 with an applied external field of $H_x = 20$ mT, current densities of $j_C = 2.604 \times 10^{12}$ A/m^2, and a damping constant of (**a**) $\alpha = 0.02$ or (**b**) $\alpha = 0.03$. Material parameters are taken from [17].

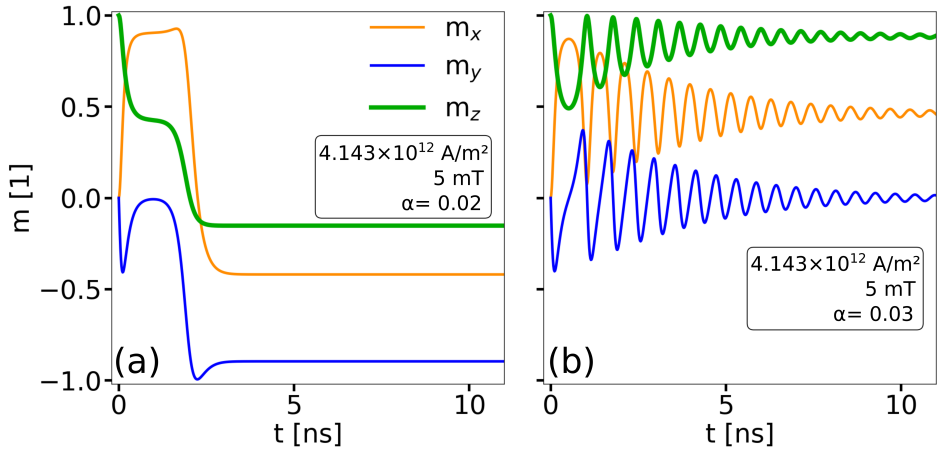


Figure 3. Time evolution of the magnetization of the system depicted in Figure 1 with an applied external field of $H_x = 5$ mT, current densities of $j_C = 4.143 \times 10^{12}$ A/m^2, and a damping constant of (**a**) $\alpha = 0.02$ or (**b**) $\alpha = 0.03$. Material parameters are taken from [17].

To demonstrate the dependence of the critical current on damping, we calculate it at several values of the external magnetic field. Figure 4a shows one of the central results: pronounced critical current density $j_{\text{crit}}(\alpha)$ dependence on α, for $H_x = 0, 5, 10, 20$ mT. A substantial dependence of the critical current on damping is most pronounced at large magnetic fields. At $H_x = 20$ mT, the critical current density of $j_{\text{crit}} = 2.6 \times 10^{12}$ A/m^2 at weak damping increases by a factor of 1.5 to $j_{\text{crit}} = 4 \times 10^{12}$ A/m^2 in the overdamped system with $\alpha > 1$. The dependence of the critical current density on the external magnetic field is shown in Figure 4b, for several α values. It demonstrates a linear decrease with

increasing field strength, with the analytical prediction (1) recovered only in overdamped systems ($\alpha > 1$).

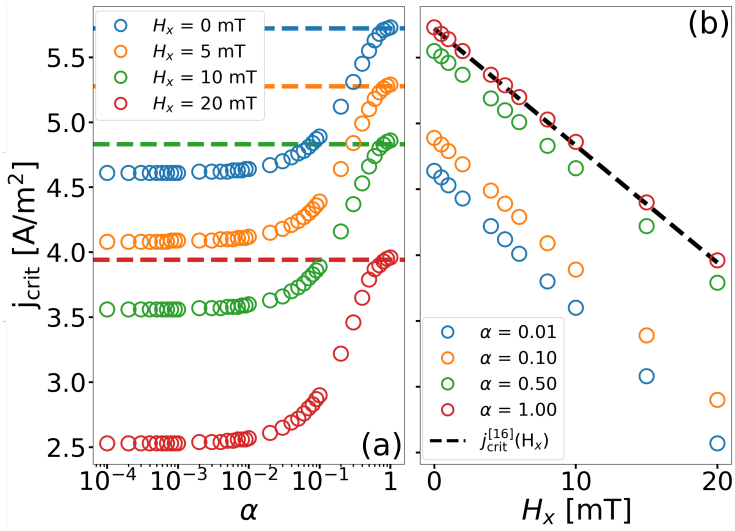


Figure 4. Critical current j_{crit} for the SOT device from Figure 1. Circles indicate the numerical results. The dashed line shows the result from Equation (1), which is not dependent on α and represents an infinitely damped system. (**a**) j_{crit} as a function of the damping constant for applied external fields of $H_x = 0$, 5, 10 and 20 mT. (**b**) j_{crit} as a function of external field H_x for a damping constant of $\alpha = 0.01$, 0.1, 0.5 or 1.0.

We note that $\alpha > 1$ is not physically realized in heavy metal/CoFeB bilayers. It serves as a mathematical limit describing the magnetization relaxing to the energy minimum state at a particular current. The first precessional overshooting above the minimum is suppressed, and the threshold reduces to the damping-independent expression (1), thereby appearing as the strong-damping endpoint of the present framework.

All results are obtained at zero temperature. At finite temperatures, the initial magnetization is instead thermally distributed about the pole, and a stochastic thermal field $\mathbf{H}_{th}$ acts throughout the current pulse and consequent relaxation. An analysis of thermal effects will be reported elsewhere [23].

3. Steady-State Landscape

To understand the damping dependence of the critical current, we first consider the steady-state solutions of Equation (2) for $\beta = 0$ and $\boldsymbol{\sigma} = -\hat{\mathbf{y}}$, corresponding to $\theta_{SH} > 0$. We call a solution of the LLG equation under the applied current a steady-state solution if $\partial \mathbf{m}/\partial t = 0$ in the current-driven LLG Equation (2). We reserve the term "stationary" for the zero-current stationary states only. The steady states are the fixed points of the driven dynamics, and the transient magnetization behavior is a damped precession about a stable one of them.

The steady-state solutions $\partial \mathbf{m}/\partial t = 0$ are obtained from the torque balance equation:

$$\mathbf{m} \times \mathbf{H}_{\text{eff}} = -B_{\text{SOT}}\, \mathbf{m} \times (\mathbf{m} \times \boldsymbol{\sigma}). \tag{5}$$

For $H_x = 0$, Equation (5) yields two families of solutions [24]. The first family $\mathbf{m}_{1,2}$ corresponds to $m_y = \pm 1$.

$$\mathbf{m}_{1,2} = (0,\ \pm 1,\ 0) \tag{6}$$

The branches $\mathbf{m}_{1,2}$ have the magnetization parallel ($\mathbf{m}_1 = \boldsymbol{\sigma}$, with $m_y = -1$) and anti-parallel ($\mathbf{m}_2 = -\boldsymbol{\sigma}$, with $m_y = 1$) to the spin current polarization $\boldsymbol{\sigma}$, so the SOT is exactly zero.

The second family of stationary states corresponds to $m_y = 0$. It consists of four partly out-of-plane branches with $m_z \neq 0$. The relation between m_z and m_x depends on the current density j_C and the effective magnetic anisotropy field H_K and can be analytically determined for $H_x = 0$. The four solutions are

$$\begin{aligned} \mathbf{m}_{4\pm1} &= \left(\mp \frac{B_{\mathrm{SOT}}/H_K}{\sqrt{k_+}},\ 0,\ \mp\sqrt{k_+} \right), \\ \mathbf{m}_{5\pm1} &= \left(\mp \frac{B_{\mathrm{SOT}}/H_K}{\sqrt{k_-}},\ 0,\ \mp\sqrt{k_-} \right), \end{aligned} \tag{7}$$

with odd and even indices corresponding to plus (shown with filled circles) and minus (open circles) signs, respectively, and

$$k_\pm = \frac{1 \pm \sqrt{1 - 4(B_{\mathrm{SOT}}/H_K)^2}}{2}. \tag{8}$$

Figure 5a shows the steady-state solutions depicted as circles, which are labeled according to the steady-state solutions presented in Equations (6) and (7).

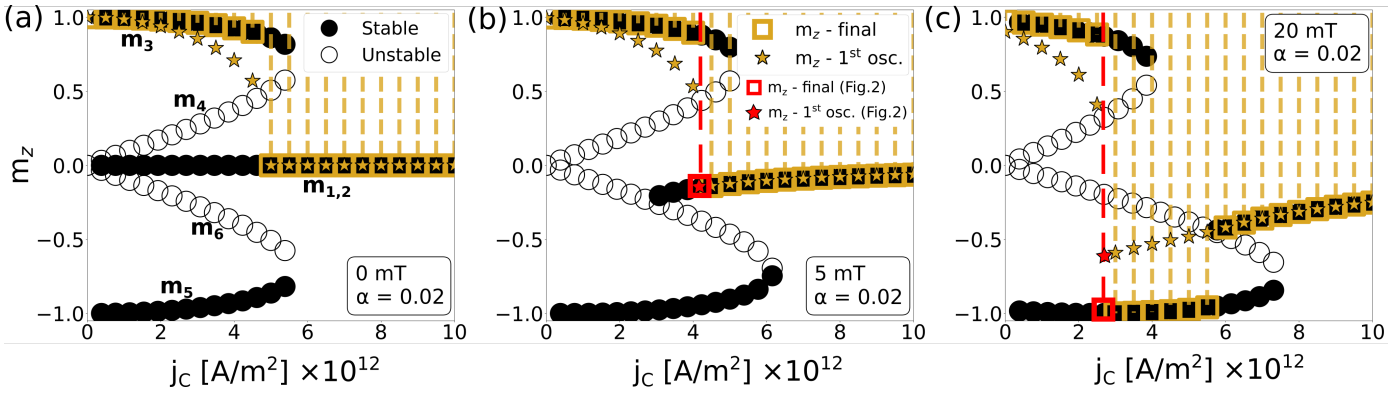


Figure 5. Switching dynamics of the SOT device depicted in Figure 1 with applied external fields of (**a**) $H_x = 0$ mT and (**b**,**c**) $H_x = 5$ mT. The m_z-component of the stable and unstable steady-state solutions are depicted as black and empty circles, respectively. In (**a**) the steady-state branches are labeled according to Equations (6) and (7). The results of dynamic simulations are depicted as yellow stars and yellow empty squares for (**a**,**b**) $\alpha = 0.02$ and (**c**) $\alpha = 1.00$. The yellow empty squares depict the final state of m_z while the current is still on. The yellow stars depict the m_z-amplitude of the first oscillation of the magnetization after onset of the current pulse. The red empty square and red star in (**b**) correspond to the results from Figure 3a, respectively, and mark the critical current for $H_x = 20$ mT and $\alpha = 0.02$.

To determine the stability of the steady-state solutions, we follow [18] by adding a small perturbation to the steady-state solution and evaluating the time evolution of the perturbation. The steady state is stable only if the perturbation relaxes back to it. The stability of the steady-state branch m_i is addressed by linearizing Equation (2) around $\mathbf{m}_i$ on the tangent plane of the unit sphere and evaluating the eigenvalues of the resulting Jacobians. The state is stable when both eigenvalues have negative real parts. A detailed formal stability analysis is presented in Appendix B. Stable and unstable steady-state solutions are marked as black filled and empty circles in Figure 5, respectively.

The solution $\mathbf{m}_1$, depicted as black filled circles in Figure 5a, exists at every current density. It is stable against a small perturbation about the steady-state position $m_y = -1$ if $B_{\mathrm{SOT}} > \alpha H_K/2$ (Appendix B). In the low-damping regime of interest, this threshold lies well below any switching current. It is expected, as the SOT enforces the magnetization to orient along the spin current polarization $\sigma = -\hat{\mathbf{y}}$. In contrast, the solution $\mathbf{m}_2$ is unstable

if perturbed away from $m_y = 1$ because the SOT acts to move the magnetization toward a stable position.

As for the out-of-plane family of solutions, the branches with odd indices, $\mathbf{m}_{3,5}$, are stable, while the branches with even indices, $\mathbf{m}_{4,6}$, are unstable. Solutions exist if $|B_{\mathrm{SOT}}/H_{\mathrm{K}}| \leq 1/2$. The odd and even branches merge pairwise at $k_+ = k_- = 1/2$ when $|B_{\mathrm{SOT}}/H_K^{\mathrm{eff}}| = 1/2$ (Figure 5a). We note that the merging current happens at the critical current density (1) with $H_x = 0$ [16]. Physically, the merging point of the perpendicular branches corresponds to the energy barrier vanishing. In the current-driven landscape the near-perpendicular attractor $\mathbf{m}_3$ is separated from the switched basin of attraction by the unstable branch $\mathbf{m}_4$, which plays the role of the barrier. The damping-like torque tilts the energy landscape. At the critical current (1) $\mathbf{m}_3$ and $\mathbf{m}_4$ merge and the barrier vanishes. The energy landscape of the current-driven system with applied external magnetic field is presented in Appendix A.

Figure 5b,c show the m_z-components for steady-state branches as a function of the applied current density for the external field $H_x = 5$ mT. We observe that for $H_x > 0$, the analytical expressions for $\mathbf{m}_{1,2}$ (6) evolve to

$$\mathbf{m}_{1,2} = \left(-\frac{H_K H_x}{B_{\mathrm{SOT}}^2},\ \mp\sqrt{1 - \left(\frac{H_K H_x}{B_{\mathrm{SOT}}^2}\right)^2 - \left(\frac{H_x}{B_{\mathrm{SOT}}}\right)^2},\ -\frac{H_x}{B_{\mathrm{SOT}}} \right). \tag{9}$$

These solutions only exist if

$$\left(H_{\mathrm{K}} H_{\mathrm{x}}/B_{\mathrm{SOT}}^2\right)^2 + \left(H_{\mathrm{x}}/B_{\mathrm{SOT}}\right)^2 \leq 1. \tag{10}$$

This explains the absence of $\mathbf{m}_{1,2}$ at low current densities beyond the crossing with the $\mathbf{m}_5$ branch. The branches $\mathbf{m}_{1,2}$ (9) increasingly shift into the lower hemisphere with increasing external magnetic field values, in agreement with Figure 5b.

Although the solutions $\mathbf{m}_{3-6}$ are still characterized by $m_y = 0$ even if $H_x \neq 0$ [16], the analytical solution requires knowing the roots of the quartic equation. The solutions $\mathbf{m}_{3-6}$ shown in Figure 5b behave differently in the upper and lower hemispheres at $H_x = 5$ mT. A contraction towards lower current densities of the existence domain for $\mathbf{m}_{3,4}$ in the upper hemisphere with increased H_x can be observed. This moves the merging point of $\mathbf{m}_3$ and $\mathbf{m}_4$ towards lower current densities. In contrast, an expansion of the existence domain for $\mathbf{m}_{5,6}$ in the lower hemisphere is observed.

4. First-Oscillation-Driven Switching

We now investigate the magnetization dynamics after the current is turned on. The initial magnetization is always along the positive z-axis, $\mathbf{m} = \hat{\mathbf{z}}$. We first consider the case of low damping with $\alpha = 0.02$. The m_z-position of the initial largest magnetization deviation after the current onset is marked with the yellow star symbols in Figure 5. When the current is small, the magnetization only slightly deviates from its initial position. After the initial, largest deviation, the magnetization undergoes damped oscillations around the nearest stable steady-state solution $\mathbf{m}_3$ and converges toward $\mathbf{m}_3$ in the upper hemisphere, shown as yellow empty squares.

For larger current densities, the SOT is sufficiently strong to make the initial deviation reach the unstable branch $\mathbf{m}_4$ and go beyond it. This results in a qualitative change of the magnetization dynamics. In this case the magnetization reaches an alternative basin of attraction and converges to the alternative steady-state solution $\mathbf{m}_1$, which is in the lower hemisphere for $H_x > 0$. Once the current is turned off, the magnetization from the $\mathbf{m}_1$ state relaxes to the stationary state $\mathbf{m} = -\hat{\mathbf{z}}$ anti-parallel to the initial state $\mathbf{m} = \hat{\mathbf{z}}$.

Figure 5b demonstrates that, at currents larger than the critical one shown in red, the magnetization is switched to the stationary $\mathbf{m}_1$ branch. The time-dependent magnetization dynamics at the critical current density are shown in Figure 3a. The m_z component, after developing a plateau when crossing the unstable branch $\mathbf{m}_4$, proceeds to the final stationary state without oscillations. This is the behavior usually expected in SOT switching.

In contrast to the traditional SOT switching picture, the critical current at which the switching appears is lower than that given by Equation (1), which was determined in [16] by the condition of absence of $\mathbf{m}_{3,4}$, beyond which the only stable state toward which the magnetization can be pushed by the SOT is $\mathbf{m}_1$. As we demonstrated, the critical current density is determined by the initial magnetization swing and initial magnetization dynamics, which are both damping-dependent. This explains why, at the stronger damping $\alpha = 0.03$, the current density is no longer sufficient to push the magnetization beyond the unstable branch $\mathbf{m}_4$, and switching is therefore absent, as shown in Figure 3b.

According to the analysis above, the critical current is determined by whether the first oscillation of the magnetization after current onset can reach and overcome the unstable stationary solution. This is a dynamic process that clearly depends on damping. As the unstable steady-state branch is approached, the magnetization dynamics slow down, resulting in plateau behavior in the magnetization time dependence in Figure 3a. The critical current value achieved at $\alpha = 0.02$ is not sufficient to overcome the unstable branch at $\alpha = 0.03$, as confirmed in Figure 3b. The initial dynamics and the first oscillation amplitude with respect to the steady-state landscape lower the critical current density compared to Equation (1), in agreement with the earlier study [17] and experiments [25,26].

The dependence of the switching current on α also explains why Equation (1) is recovered only for large damping $\alpha > 1$. In an overdamped system, the magnetization is steadily pushed by the SOT towards the stable steady state $\mathbf{m}_3$ in the upper hemisphere as shown in Figure 5c. As there is almost no inertia, the magnetization is locked in $\mathbf{m}_3$ and stays there, unless the current is strong enough that the stable solution $\mathbf{m}_3$ does not exist (Figure 5c). Thus, in an overdamped system, the stable branch $\mathbf{m}_3$ itself has to vanish to facilitate switching. As this corresponds to the definition of the critical current in [16], we recover the well-known result (1) as a limiting case of strong damping from our general approach.

5. Field-like Torque and Instability-Driven Switching

We include the field-like torque (FLT) by setting $\beta \neq 0$ in Equation (2). The torque balance equation becomes

$$\begin{aligned} &\mathbf{m} \times (H_K m_z \, \hat{\mathbf{z}} + H_x \, \hat{\mathbf{x}}) = \\ &- B_{\mathrm{SOT}} \, \mathbf{m} \times (\mathbf{m} \times (\boldsymbol{\sigma})) - \beta B_{\mathrm{SOT}} \, \mathbf{m} \times (\boldsymbol{\sigma}). \end{aligned} \tag{11}$$

Figure 6 shows the m_z-component and stability of the steady-state branches for $\beta = \pm 0.2$, $\alpha = 0.02$, and $H_x = 5$ mT. The branches $\mathbf{m}_{1,2}$ are split under the influence of FLT. The branch $\mathbf{m}_1$ oriented nearly along $\boldsymbol{\sigma} = -\hat{\mathbf{y}}$ is in the lower hemisphere and remains stable. However, its range of existence strongly depends on the sign of β. For $\beta < 0$, it exists over the entire current range (Figure 6b), while for $\beta > 0$, it sets in at a finite current value (Figure 6a).

At $\beta > 0$, the steady-state landscape looks similar to that at $\beta = 0$ and the switching proceeds according to the first-oscillation-driven switching discussed previously. At $\beta < 0$, the branch $\mathbf{m}_3$ becomes unstable at $j_C > 3 \times 10^{12}$ A/m^2. As the nearest stable branch at $j_C > 3.0 \times 10^{12}$ A/m^2 is $\mathbf{m}_1$, the magnetization is driven towards it regardless of the

amplitude of the initial deviation (Figure 6b). This completely modifies the switching behavior, enabling instability-driven switching.

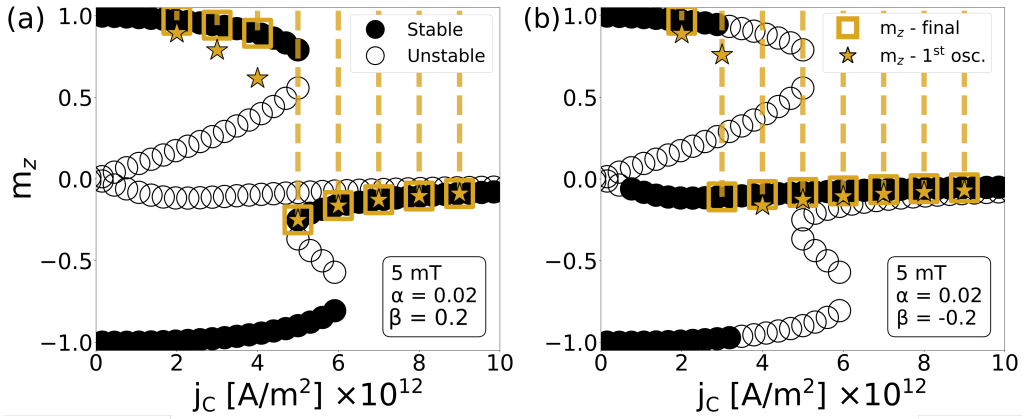


Figure 6. The m_z-component of the magnetization **m** of the steady-state solutions in an SHE-driven SOT-MRAM device with applied external field of $H_x = 5$ mT, including field-like torques with $\beta = \pm 0.2$.

As the current at which the instability appears is lower than the critical current at $\beta = 0$, negative β facilitates magnetization switching at lower current densities.

Figure 7 illustrates the difference between first-oscillation-driven and instability-driven switching. The left panel shows the time evolution of the magnetization components for $j_C = 4.6 \times 10^{12}$ A/m^2 at $\beta = 0.2$ and $\alpha = 0.02$ and the right panel shows the corresponding evolution for $j_C = 3 \times 10^{12}$ A/m^2 at $\beta = -0.2$ and $\alpha = 0.02$ (see also Figure 6a and Figure 6b, respectively). In the left panel, magnetization reversal is governed by the first-oscillation-driven mechanism; however due to FLT, the critical switching current is higher than without FLT (see Figure 3). In the right panel, initial magnetization oscillations grow due to the instability of the steady state until the magnetization switches to the stable SOT-dominant branch. Here the critical current density is reduced compared to the case without FLT; however due to the small growth rate of the oscillation, the total switching time is longer.

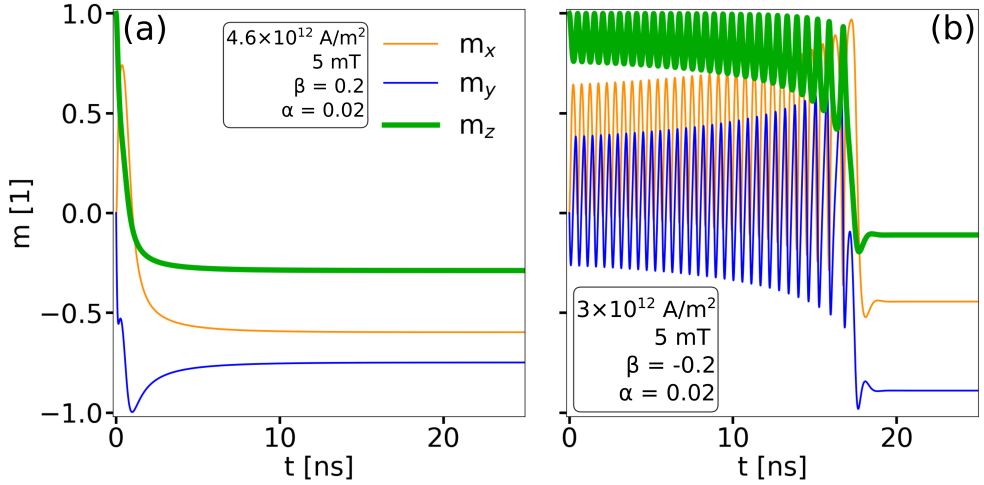


Figure 7. Time evolution of the magnetization for $\beta = \mp 0.2$ and current densities of (**a**) $j_C = 4.6 \times 10^{12}$ and (**b**) $j_C = 3 \times 10^{12}$ A/m^2. Applied external field: $H_x = 5$ mT; damping constant: $\alpha = 0.02$.

Figure 8 shows the damping-dependent critical current $j_{\mathrm{crit}}(\alpha)$ for various H_x and β values. For $\beta = 0.2$, a decrease in the switching current to a smaller finite value is observed for weak damping, in complete analogy to the case of $\beta = 0$. In contrast, for $\beta = -0.2$,

the instability-driven critical current density decreases more rapidly for weak damping, $\alpha < 0.01$, following a universal dependence, depicted by dashed lines in Figure 8b, which follow the expression for the critical current density [18]:

$$j_{\text{crit}}^{\text{FLT}} \approx \frac{2eM_S d_f}{\hbar\theta_{SHE}} \sqrt{\frac{\alpha(2H_K^2 - H_x^2)}{-\beta(2-\alpha\beta)}}. \tag{12}$$

This expression is valid only for $\beta < 0$. We note that we use a more common sign convention for β [19] defined by (11), which is opposite to that in [18,27].

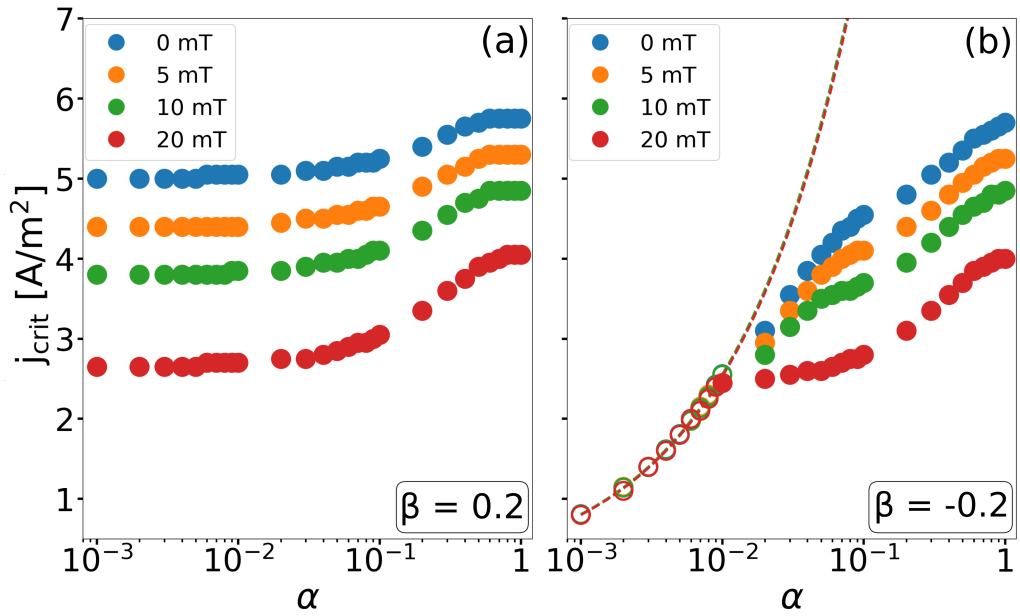


Figure 8. Critical current j_{crit} for the SOT device including the field-like torque with (**a**) $\beta = 0.2$ and (**b**) $\beta = -0.2$. Circles show the results of numerical simulations. Filled and empty circles indicate whether magnetization reversal is governed by the first-oscillation-driven or instability-driven mechanism, respectively. The dashed lines in (**b**) depict the analytical solution from (12).

Figure 9 shows the β-dependence of the critical current for a system with $H_x = 20$ mT and $\alpha = 0.01, 0.1$ and 1.0. As discussed earlier, field-like torque with $\beta < 0$ supports switching, resulting in lower switching currents. Increasing $\beta > 0$ initially leads to a slight increase in the critical current density, followed by its reduction at larger β, in agreement with earlier studies [17]. Although less pronounced than for $\beta < 0$, the dependence on damping is clearly visible. It originates from first-oscillation-driven switching, for which less current is required to overcome the unstable steady state $\mathbf{m}_4$ at low damping.

We note that in addition to the FLT generated via the SHE, a strong field-like torque component at the FM/HM interface is generated by the Rashba–Edelstein effect [20], so even by investigating one of the most promising interfaces between CoFeB and W, different β values were reported [27–30].

For a particular stack with negative β, both mechanisms are available. The observed critical current is set by whichever switches the magnetization first:

$$j_c(\alpha) = \min\left(j_c^{\text{osc}}(\alpha),\ j_c^{\text{FLT}}(\alpha)\right), \tag{13}$$

with j_c^{osc} being the first-oscillation-driven threshold and j_c^{FLT} the instability-driven threshold of Equation (12).

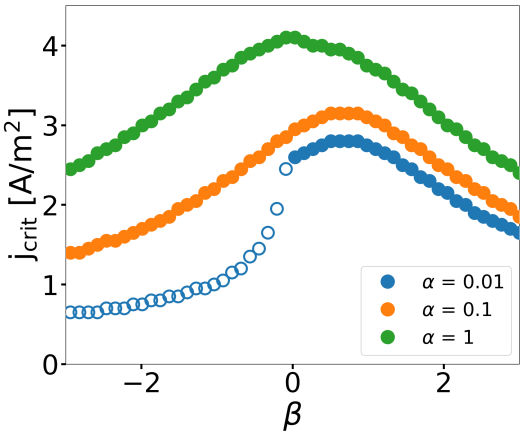


Figure 9. β-dependence of j_{crit} for the SOT device including the field-like torque. Circles show the results of numerical simulations for $H_x = 20$ mT and $\alpha = 0.01, 0.1$ and 1.0. Filled and empty circles indicate whether magnetization reversal is governed by the first-oscillation-driven or instability-driven mechanism, respectively.

In recent experimental studies [28] of the critical current in Ta/CoFeB and W/CoFeB stacks, the instability-driven mechanism [18] was used to explain the experimental dependencies on the external magnetic field. Both stacks were characterized with relatively large β values of -1.06 and -0.3 in our sign convention. Regardless of the relatively large size of these devices (80 nm), the macrospin model fitted the experiment surprisingly well. To determine the critical switching current, 1 ms pulses were used. The current dependence on the pulse duration t_p for the instability-driven mechanism is given by

$$j_c^2(t_p) = j_{C|FLT}^2 \, (1 + \tau_0/t_p), \tag{14}$$

where $\tau_0 = (1 + \alpha^2)/(\gamma \alpha H_K)$ is the characteristic free-layer Gilbert damping time independent of β (Appendix B). Although the critical threshold current $j_{C|FLT}^2$ corresponds to the limit $t_p \to \infty$, it is a common prefactor in (14). This is in good agreement with [28] in terms of the experimentally determined critical currents at finite t_p. Reducing the critical current at fixed t_p reduces the switching energy, which scales as $E \propto j_C^2 t_p = j_{C|FLT}^2 \, (t_p + \tau_0)$. As the critical current scales with $j \propto \sqrt{\alpha/(-\beta)}$ in systems with low damping, large negative β favors the critical current reduction and the switching energy at the fixed pulse length.

6. Discussion

Although the macrospin model does not include spatially nonuniform effects such as domain nucleation and propagation, edge demagnetization, and nonuniform torques, it allows the experimental results [28] to be fitted correctly. The nonuniform effects may reduce the energy barrier between the two states, thereby reducing the thermal stability of the devices, and should be avoided. To reduce nonuniform effects, the geometric cell size should be minimized to approach the single-uniform-domain limit. At the same time, the uniaxial magnetic anisotropy should be increased to maintain the devices' thermal stability. The macrospin model is expected to work even better and could become indispensable for determining the fundamental switching mechanisms in such ultra-scaled devices.

In contrast, the switching current reduction achieved by the two mechanisms described is due to dynamic effects caused by the current. The device's thermal stability is not compromised, as the energy barrier in the absence of current remains unchanged. The field-like torque helps reduce the switching current, especially due to the instability-driven mechanism in the experimentally relevant case of large negative β values [19,27,28].

We note, however, that at low currents, the switching time increases for the instability-driven mechanism.

Apart from interpreting the switching behavior and helping determine the switching current, the steady-state landscape predicts the state to which the magnetization relaxes if the current exceeds the critical value. The model predicts that the steady-state solution $\mathbf{m}_1$ in Figure 6 approaches the top of the anisotropy barrier at $m_z = 0$ for large currents. Since $\mathbf{m}_1$ is the starting point of the relaxation process after the current is switched off, the magnetization may back-switch to its initial state at finite temperature. This recently observed back-switching effect in realistic devices [29,31] is fully consistent with our model and its steady-state analysis.

7. Conclusions

We have developed a framework for exploring deterministic magnetization switching in perpendicular SOT-MRAM devices, built on the steady-state landscape of the current-driven macrospin LLG equation and the transient dynamics following current injection, from which two physically distinct switching mechanisms emerge.

In the first-oscillation-driven mechanism, the critical current is determined by whether the amplitude of the initial m_z deviation reaches and overcomes an unstable steady-state branch that acts as a separatrix between basins of attraction to two distinct steady-state branches. Because this overshoot reflects the balance between SOT work and Gilbert dissipation during the first precession, the threshold is inherently α-dependent as lower damping yields a larger overshoot and a lower critical current. It recovers the damping-independent result of [16] only if $\alpha > 1$, where the first oscillation is fully damped, and switching requires reaching the current at which the unstable steady-state branch $\mathbf{m}_4$ ceases to exist. In this picture, the plateau reported in [17] is an important indication of switching, as it arises from dynamical slowing near the unstable branch at minimum current. The damping dependence of the switching current shows that the initial dynamics are decisive for overcoming the unstable branch. Even a slight increase in α suppresses switching.

The instability-driven mechanism becomes operative when a field-like torque with negative β is included. It destabilizes the equilibrium branch in the upper hemisphere itself, so that a small current-induced perturbation from the initial magnetization position grows over successive compounding cycles, until the trajectory eventually crosses the equator and ends on the stable solution in the lower hemisphere. At finite β, the observed critical current is the minimum over both mechanisms.

The two-mechanism picture provides a practical guide for reducing the switching current in perpendicular SOT-MRAM design. The damping constant α is the primary lever on the first-oscillation-driven threshold through the first oscillation amplitude, while the field-like torque ratio β independently introduces the instability-driven threshold. Low damping is still required to reduce the current substantially.

Expression (1) describes the minimal current density required for switching. It has been regarded as a hard limit with a single tuning parameter, the external magnetic field, hindering the need to reduce the current. The steady-state landscape, however, enables a path towards systematic reduction of the critical switching current density in perpendicular SOT-MRAM.

Author Contributions: Conceptualization, methodology, software, and formal analysis, B.P.; validation and writing—original draft, B.P. and V.S.; supervision, V.S.; funding acquisition and writing—review and editing, S.S. All authors have read and agreed to the published version of the manuscript.

Funding: This research received no external funding

Data Availability Statement: The simulation code used in this study is available from the corresponding author upon reasonable request. The finite-element micromagnetic framework developed in our group is publicly available at https://gitlab.tuwien.ac.at/novomemlog/viennaspinmag (accessed on 11 September 2026).

Acknowledgments: The authors acknowledge TU Wien Bibliothek for financial support through its Open Access Funding Program.

Conflicts of Interest: The authors declare no conflict of interests.

Appendix A. Energy Landscape

In the quasi-static overdamped limit, the kinetic energy is suppressed, and the magnetization remains within the x–z plane, minimizing the magnetic energy in the upper hemisphere ($m_y = 0$). Although the damping-like SOT is not conservative, in this one-dimensional case it can be used to define an effective energy of the magnetization under current $\varepsilon(\theta)$ as a function of the polar angle θ between the magnetization and the easy magnetization axis z as follows [32]:

$$\varepsilon(\theta) = -K_\mathrm{u} \cos^2\theta \; - \; M_S H_x \sin\theta \; - \; M_S B_\mathrm{SOT}\, \theta, \tag{A1}$$

where $K_\mathrm{u} = \frac{1}{2} M_S B_K$ is the uniaxial anisotropy density ($B_K = \mu_0 H_K$ is the effective anisotropy field), and $B_\mathrm{SOT} = \hbar \theta_\mathrm{SHE}\, j_C / (2 e M_S d_f)$ is the damping-like torque amplitude.

Figure A1 shows the energy landscape in the upper hemisphere for a current-driven system with $\beta = 0$, for several applied current densities j_C and applied external fields $H_x = 5$ and 20 mT. Energy minima and maxima are depicted as circles and triangles, respectively. The energy minima correspond to the stable steady-state solutions acting as attractors. The energy maxima correspond to the unstable steady-state solutions acting as a separatrix between two energy basins. The merging points, which mark the existence limits of the steady-state branches, are depicted as squares. The current density of the merging points is the critical current density of overdamped systems from Equation (1). Beyond the critical current, no separating maxima exist, and the magnetization in the current-driven system readily switches, without having to overcome an energy barrier.

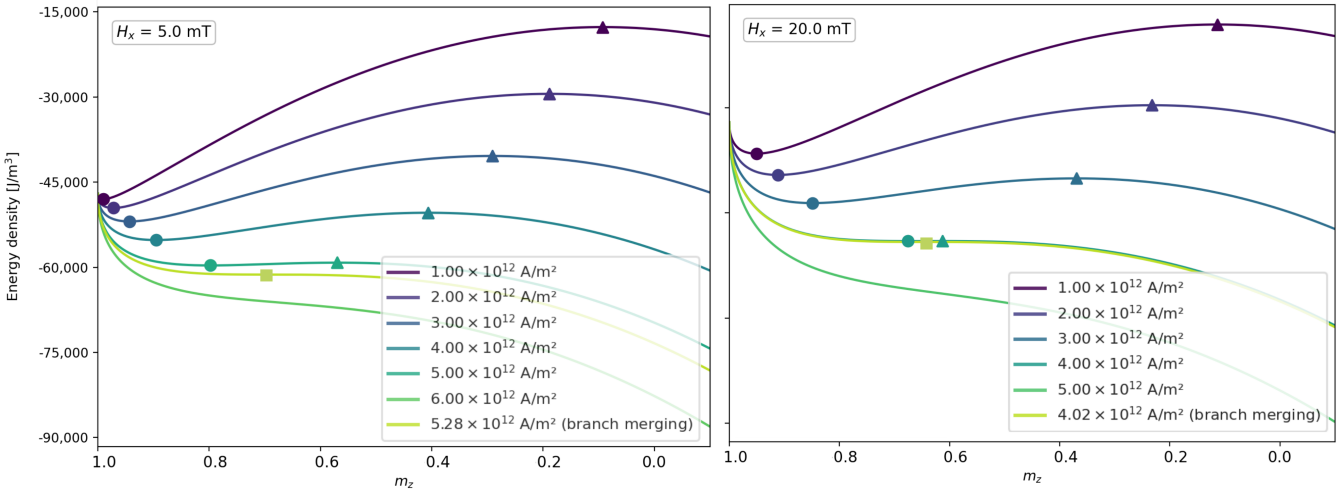


Figure A1. Outline of the energy from Equation (A1) in the upper hemisphere for a current-driven system with applied external fields of $H_x = 5$ and 20 mT for various current densities j_C. Energy minima and maxima are depicted as circles and triangles, respectively. The merging points of minima and maxima are depicted as squares.

The merging point is the simultaneous solution of $\varepsilon'(\theta) = 0$ and $\varepsilon''(\theta) = 0$,

$$\tfrac{1}{2}B_K \sin 2\theta - H_x \cos\theta - B_{\mathrm{SOT}} = 0, \qquad B_K \cos 2\theta + H_x \sin\theta = 0. \tag{A2}$$

For $H_x = 0$ the barrier disappears at $\theta = \pi/4$ (i.e., $m_z = m_x = 1/\sqrt{2}$) when $B_{\mathrm{SOT}} = B_K/2$; for a finite in-plane field, to leading order, $B_{\mathrm{SOT}}^{\mathrm{crit}} = B_K/2 - H_x/\sqrt{2}$. This yields the critical current density

$$j_{\mathrm{crit}} = \frac{2eM_S d_f}{\hbar\theta_{\mathrm{SHE}}}\left(\frac{B_K}{2} - \frac{H_x}{\sqrt{2}}\right), \tag{A3}$$

which coincides with Equation (1), at $H_x = 0$. The barrier-removal condition $B_{\mathrm{SOT}} = B_{\mathrm{SOT}}^{\mathrm{crit}}$ is the energy-landscape form of the saddle-node $\det J_{2D} = 0$ in Appendix B, and is the energy counterpart of the oscillatory (field-like-torque) instability, which instead follows from $\mathrm{tr}\, J_{2D} = 0$. Being derived in the quasi-static limit, this picture is exact where the damping-independent expression (1) applies for $\alpha \gtrsim 1$.

Appendix B. Stability Analysis

We add a small perturbation to a steady-state solution $\mathbf{m}(t) = \mathbf{m}_0 + \delta\mathbf{m}(t)$. The constraint $|\mathbf{m}| = 1$ requires $\mathbf{m}_0 \cdot \delta\mathbf{m} = 0$, meaning perturbations lie on the tangent plane to the unit sphere at $\mathbf{m}_0$. We introduce two orthogonal unit vectors $\{\hat{e}_1, \hat{e}_2\}$ on this plane and write

$$\delta\mathbf{m} = u_1\,\hat{e}_1 + u_2\,\hat{e}_2. \tag{A4}$$

Linearizing the LLG equation $\partial\mathbf{m}/\partial t = \mathbf{f}(\mathbf{m})$ around $\mathbf{m}_0$,

$$\frac{\partial\delta\mathbf{m}}{\partial t} = \mathbf{J}(\mathbf{m}_0)\,\delta\mathbf{m}, \qquad \mathbf{J}(\mathbf{m}_0) = \left.\frac{\partial\mathbf{f}}{\partial\mathbf{m}}\right|_{\mathbf{m}_0}, \tag{A5}$$

with the Jacobian $\mathbf{J}$. Projecting onto the tangent-plane basis gives the 2×2 system

$$\frac{d}{dt}\begin{pmatrix} u_1 \\ u_2 \end{pmatrix} = \begin{pmatrix} \hat{e}_1 \cdot \mathbf{J}\hat{e}_1 & \hat{e}_1 \cdot \mathbf{J}\hat{e}_2 \\ \hat{e}_2 \cdot \mathbf{J}\hat{e}_1 & \hat{e}_2 \cdot \mathbf{J}\hat{e}_2 \end{pmatrix}\begin{pmatrix} u_1 \\ u_2 \end{pmatrix} \equiv \mathbf{J}\begin{pmatrix} u_1 \\ u_2 \end{pmatrix}. \tag{A6}$$

The solution is $\mathbf{u}(t) = c_1 e^{\lambda_1 t}\mathbf{v}_1 + c_2 e^{\lambda_2 t}\mathbf{v}_2$, with λ_i and $\mathbf{v}_i$ representing the eigenvalues and eigenvectors of the Jacobian $\mathbf{J}$. The steady state is stable if both eigenvalues have negative real parts, which requires $\mathrm{tr}(\mathbf{J}) < 0$ and $\det(\mathbf{J}) > 0$.

The two eigenvalues,

$$\lambda_\pm = \tfrac{1}{2}\left(\mathrm{tr}\,\mathbf{J} \pm \sqrt{\mathrm{tr}^2\mathbf{J} - 4\det\mathbf{J}}\right), \tag{A7}$$

make the two possible ways of losing stability explicit. A branch is stable while $\mathrm{tr}\,\mathbf{J} < 0$ and $\det\mathbf{J} > 0$, and it can destabilize in two qualitatively distinct ways that depend on the sign of the discriminant $\mathrm{tr}^2(\mathbf{J}) - 4\det(\mathbf{J})$.

(i) Static. $\mathrm{tr}^2(\mathbf{J}) - 4\det(\mathbf{J}) > 0$ and $\det(\mathbf{J}) \to 0$ with real eigenvalues. One eigenvalue passes through zero and the destabilization is monotonic. This is the merging of the two out-of-plane branches $\mathbf{m}_3$ and $\mathbf{m}_4$, or $\mathbf{m}_5$ and $\mathbf{m}_6$. It corresponds to the removal of the energy barrier and yields the damping-independent threshold Equation (1).

(ii) Dynamic. $\mathrm{tr}^2(\mathbf{J}) - 4\det(\mathbf{J}) < 0$ and $\mathrm{tr}(\mathbf{J}) \to 0$ at $\det(\mathbf{J}) > 0$. The square root in Equation (A7) is then imaginary, so the eigenvalues are a complex-conjugate pair $\lambda_\pm = \pm i\sqrt{\det\mathbf{J}}$. Below this threshold, the magnetization, after initial perturbation, performs damped oscillations that converge back to the steady state. Beyond this threshold, the oscillations grows. The steady state still exists, but it ceases to be stable.

This type of destabilization is activated by the field-like torque, and imposing $\mathrm{tr}(\mathbf{J}) = 0$ yields the analytic instability-driven threshold derived below.

We first apply this method to the in-plane steady states $\mathbf{m}_{1,2} = \pm\hat{y}$, whose tangent plane has basis $(x,\, 0,\, z)^T$. Linearizing the LLG equation around $\mathbf{m}_0$ and using $s = \pm 1$ we obtain

$$\frac{\partial \delta\mathbf{m}}{\partial t} + \alpha\, \mathbf{m}_0 \times \frac{\partial \delta\mathbf{m}}{\partial t} = -\gamma\, m_z H_K\, s\, \hat{x} + \gamma B_{\mathrm{SOT}}\, s\, (m_x\, \hat{x} + m_z\, \hat{z}). \tag{A8}$$

By using $\mathbf{m}_0 \times \delta\dot{\mathbf{m}} = s\,(\dot{z},\, 0,\, -\dot{x})^T$, we obtain

$$\dot{x} - \alpha s\, \dot{z} = s\, \gamma\, (B_{\mathrm{SOT}}\, x - H_K\, z), \tag{A9a}$$

$$\dot{x} + \alpha s\, \dot{z} = s\, \gamma\, B_{\mathrm{SOT}}\, z. \tag{A9b}$$

Solving for $\dot{x}$ and $\dot{z}$ gives the Jacobian

$$J = \begin{pmatrix} s\, B_{\mathrm{SOT}} & -s\, H_K + \alpha\, B_{\mathrm{SOT}} \\ -\alpha\, B_{\mathrm{SOT}} & \alpha\, H_K + s\, B_{\mathrm{SOT}} \end{pmatrix}, \tag{A10}$$

with

$$\mathrm{tr}(J) = 2s\, B_{\mathrm{SOT}} + \alpha\, H_K, \qquad \det(J) = (1+\alpha^2)\, B_{\mathrm{SOT}}^2. \tag{A11}$$

Since $\det(J) = (1+\alpha^2) B_{\mathrm{SOT}}^2 > 0$ always, case (i) is inaccessible here and the stability of the in-plane states is governed by the trace alone. $\mathrm{tr}(J) < 0$ requires $s\, B_{\mathrm{SOT}} < -\frac{1}{2}\alpha H_K$. Because $B_{\mathrm{SOT}} > 0$ and $H_K > 0$, this holds only for $s = -1$, giving $B_{\mathrm{SOT}} > \frac{1}{2}\alpha H_K$, whereas for $s = +1$ it reads $B_{\mathrm{SOT}} < -\frac{1}{2}\alpha H_K < 0$ and is never satisfied. Therefore $\mathbf{m}_1 = -\hat{y}$ is stable and $\mathbf{m}_2 = +\hat{y}$ is unstable.

The same procedure applied to the out-of-plane branches yields $\mathbf{m}_3$ and $\mathbf{m}_5$, which are stable, and $\mathbf{m}_4$ and $\mathbf{m}_6$, which are unstable. Without a field-like torque these branches destabilize through route (i): the stable branch $\mathbf{m}_3$ and the unstable branch $\mathbf{m}_4$ merge at $\det(\mathbf{J}) = 0$ and disappear, which is the barrier-removal condition from Appendix A and reproduces Equation (1).

The FLT modifies the stability of the steady-state branches. We highlight the stable out-of-plane branch $\mathbf{m}_3$. Starting from the torque balance with FLT, the components read, to leading order in B_{SOT}/H_K,

$$m_{3,x} \approx \frac{B_{\mathrm{SOT}}}{H_K}, \qquad m_{3,y} \approx -\beta\, \frac{B_{\mathrm{SOT}}}{H_K}, \qquad m_{3,z} \approx 1. \tag{A12}$$

The damping-like torque tilts the magnetization towards $\hat{x}$ while the field-like torque adds the m_y-component. Linearizing Equation (2) about this state and projecting onto the tangent plane gives, to second order in B_{SOT}/H_K,

$$\mathbf{J} = \frac{\gamma}{1+\alpha^2} \begin{pmatrix} -\alpha H_K + 2(\alpha-\beta)\, \dfrac{B_{\mathrm{SOT}}^2}{H_K} & -H_K + (1+\beta^2)\, \dfrac{B_{\mathrm{SOT}}^2}{H_K} \\ H_K - 2(1+\alpha\beta)\, \dfrac{B_{\mathrm{SOT}}^2}{H_K} & -\alpha H_K + \alpha(1+\beta^2)\, \dfrac{B_{\mathrm{SOT}}^2}{H_K} \end{pmatrix}, \tag{A13}$$

with trace and determinant

$$\mathrm{tr}(\mathbf{J}) = \frac{\gamma}{1+\alpha^2}\left[-2\alpha H_K + \left(3\alpha + \alpha\beta^2 - 2\beta\right)\frac{B_{\mathrm{SOT}}^2}{H_K}\right], \tag{A14}$$

$$\det(\mathbf{J}) = \frac{\gamma^2}{1+\alpha^2}\left[H_K^2 - \left(3+\beta^2\right)B_{\mathrm{SOT}}^2\right]. \tag{A15}$$

Equations (A14) and (A15) contain both destabilization routes. $\det(\mathbf{J})$ decreases with current and reaches zero at $B_{\mathrm{SOT}}^2 = H_K^2/(3+\beta^2)$, the merging point of the perpendicular branches. The stability criterion $\mathrm{tr}(\mathbf{J}) < 0$, on the other hand, reads

$$2\alpha H_K - \left(3\alpha + \alpha\beta^2 - 2\beta\right)\frac{B_{\mathrm{SOT}}^2}{H_K} > 0, \tag{A16}$$

so $\mathrm{tr}(\mathbf{J})$ grows with current only if $3\alpha + \alpha\beta^2 - 2\beta > 0$, which for small α requires $\beta < 0$. Setting $\mathrm{tr}(\mathbf{J}) = 0$ then gives the critical B_{SOT}:

$$B_{\mathrm{SOT}}^{\mathrm{crit}} = H_K\sqrt{\frac{2\alpha}{3\alpha + \alpha\beta^2 - 2\beta}} = H_K\sqrt{\frac{2\alpha}{-\beta\,(2-\alpha\beta) + 3\alpha}}. \tag{A17}$$

For $\beta < 0$ this crossing occurs before the determinant vanishes, so the branch becomes unstable while it still exists, which is the origin of the instability-driven mechanism. For $\beta > 0$ the trace stays negative until the branch ceases to exist at the merging point.

In the regime of interest, $\alpha \ll |\beta|$, the term 3α is negligible against -2β and Equation (A17) reduces to $B_{\mathrm{SOT}}^{\mathrm{crit}} = H_K\sqrt{2\alpha/[-\beta(2-\alpha\beta)]}$. With $B_{\mathrm{SOT}} = \hbar\theta_{\mathrm{SHE}}\, j_C/(2eM_S d_f)$ the critical current density in the field-free case is

$$j_c^{\mathrm{FLT}} = \frac{2eM_S d_f}{\hbar\,\theta_{\mathrm{SHE}}}\,H_K\sqrt{\frac{2\alpha}{-\beta\,(2-\alpha\beta)}}, \tag{A18}$$

and with an applied external field

$$j_c^{\mathrm{FLT}} \approx \frac{2eM_S d_f}{\hbar\,\theta_{\mathrm{SHE}}}\sqrt{\frac{\alpha\left(2H_K^2 - H_x^2\right)}{-\beta\,(2-\alpha\beta)}}, \tag{A19}$$

recovering the result of [18]. This threshold marks the current at which the stable state itself becomes unstable, thus enabling the instability-driven switching mechanism.

Figure A2 verifies the instability numerically and displays $\det(\mathbf{J})$ and $\mathrm{tr}(\mathbf{J})$ of the branch $\mathbf{m}_3$. The point at which $\mathrm{tr}(\mathbf{J}) = 0$ marks the onset of dynamic instability at $j_C^{\mathrm{FLT}} \approx 3.14 \times 10^{12}$ A/m^2. Beyond this current density, $\mathbf{m}_3$ becomes unstable. The point at which $\det(\mathbf{J}) = 0$ marks the point beyond which $\mathbf{m}_3$ does not exist at $j_C \approx 5.3 \times 10^{12}$ A/m^2; thus, the energy barrier vanishes.

The trace also determines how fast the instability develops. As the eigenvalues form a complex-conjugate pair at the crossing, the growth rate of the oscillation is $\mathrm{Re}\,\lambda = \frac{1}{2}\,\mathrm{tr}(\mathbf{J})$, and with $\mathcal{D} \equiv 3\alpha + \alpha\beta^2 - 2\beta$ the trace (A14) factorizes into

$$\mathrm{Re}\,\lambda = \frac{\gamma\,\mathcal{D}}{2(1+\alpha^2)H_K}\left[B_{\mathrm{SOT}}^2 - \left(B_{\mathrm{SOT}}^{\mathrm{crit}}\right)^2\right]. \tag{A20}$$

The growth rate vanishes at this threshold, so the instability-driven mechanism requires a pulse long enough for the oscillation to build up. Identifying the required pulse length with the inverse growth rate gives

$$j_c^{\mathrm{FLT}}(t_p) = \sqrt{\left(j_c^{\mathrm{FLT}}\right)^2 + \frac{b}{t_p}}, \qquad b = \frac{2\left(1+\alpha^2\right)H_K}{\gamma\,\mathcal{D}\,\zeta^2}, \qquad \zeta = \frac{\hbar\,\theta_{\mathrm{SHE}}}{2eM_S d_f}, \tag{A21}$$

where j_c^{FLT} without an argument denotes the long-pulse threshold of Equation (12), which Equation (A21) approaches over the time $b/\left(j_c^{\mathrm{FLT}}\right)^2 = (1+\alpha^2)/(\gamma\alpha H_K)$ for $H_x \ll H_K$. This is the Gilbert relaxation time of the free layer and does not depend on β: the field-like torque scales the whole curve without changing its shape.

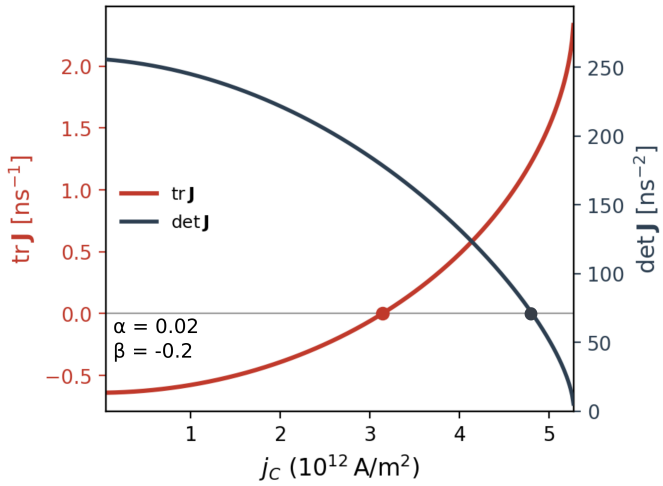


Figure A2. Trace (left axis) and determinant (right axis) of the Jacobian of the steady-state branch $\mathbf{m}_3$ for $\alpha = 0.02$ and $\beta = -0.2$. $\mathrm{tr}(\mathbf{J}) = 0$ at $j_C \approx 3.14 \times 10^{12}$ A/m^2, marking the onset of dynamic instability. $\det(\mathbf{J}) = 0$ at $j_C \approx 5.3 \times 10^{12}$ A/m^2, marking the point beyond which $\mathbf{m}_3$ has no solutions.

References

1. Hellenbrand, M.; Teck, I.; MacManus-Driscoll, J.L. Progress of Emerging Non-Volatile Memory Technologies in Industry. *MRS Commun.* **2024**, *14*, 1099–1112. [CrossRef] [PubMed]
2. Huang, P.; Di Perna, M.A.; Hwang, W.; Xue, F.; Tsai, W.; Fan, D.; Wang, S.X. Next-Generation MRAM Technologies and their emerging Roles in Artificial Intelligence. *J. Magn. Magn. Mater.* **2026**, *655*, 174308. [CrossRef]
3. Lee, P.H.; Lee, C.F.; Lin, H.J.; Lu, C.H.; Chang, Y.A.; Sanjaya, P.W.; Tsen, C.J.; Chen, K.C.; Lin, M.C.; Hung, C.J.; et al. 15.4 A 16nm 168Mb Embedded STT-MRAM with 0.0249 µm^2 Bit-Cell, Dual-Port Access, and 51.2Gb/s Read Throughput for Automotive and Edge AI Applications. In *Proceedings of the 2026 IEEE International Solid-State Circuits Conference (ISSCC), San Francisco, CA, USA, 15–19 February 2026*; IEEE: New York, NY, USA, 2026.
4. Ko, S.; Shim, J.; Park, J.H.; Lim, W.; Jung, H.; Bak, J.H.; Jeong, D.; Lee, J.W.; Whang, H.; Eom, M.; et al. Key Technologies of Scaling Embedded MRAM to 8nm Logic and Beyond for Automotive Application. In *Proceedings of the 2024 IEEE International Electron Devices Meeting (IEDM), San Francisco, CA, USA, 7–11 December 2024*; IEEE: New York, NY, USA, 2024.
5. Whang, H.S.; Ko, S.; Shim, J.C.; Lim, W.; Park, J.H.; Lee, T.Y.; Bae, G.; Lee, C.; Ryu, K.; Choi, S.; et al. World First 8nm 128Mb Embedded STT-MRAM for Automotive Application. In Proceedings of the 2025 International Electron Devices Meeting (IEDM), San Francisco, CA, USA, 6–10 December 2025.
6. Jung, H.; Song, Y.; Ko, S.; Park, J.H.; Ahn, S. Overview of Reliability in Scaling Embedded STT-MRAM. In *Proceedings of the 2025 IEEE International Reliability Physics Symposium (IRPS), Tucson, AZ, USA, 22–26 March 2025*; IEEE: New York, NY, USA, 2025.
7. Nguyen, V.; Talmelli, G.; Monteiro, M.G.; Palomino, A.; Kateel, V.; Giuliano, D.; Van Beek, S.; Meeren, N.V.; Vergel, N.F.; Wostyn, K.; et al. Achieving 1ppm Write-Error Rate in SOT-MRAM with Synthetic Antiferromagnetic Free Layer. In *Proceedings of the 2024 IEEE International Electron Devices Meeting (IEDM), San Francisco, CA, USA, 7–11 December 2024*; IEEE: New York, NY, USA, 2024.
8. Dyakonov, M.; Perel, V. Current-Induced Spin Orientation of Electrons in Semiconductors. *Phys. Lett. A* **1971**, *35*, 459–460. [CrossRef]

9. Sinova, J.; Culcer, D.; Niu, Q.; Sinitsyn, N.A.; Jungwirth, T.; MacDonald, A.H. Universal Intrinsic Spin Hall Effect. *Phys. Rev. Lett.* **2004**, *92*, 126603. [CrossRef] [PubMed]
10. Garello, K.; Yasin, F.; Couet, S.; Souriau, L.; Swerts, J.; Rao, S.; Van Beek, S.; Kim, W.; Liu, E.; Kundu, S.; et al. SOT-MRAM 300MM Integration for Low Power and Ultrafast Embedded Memories. In *Proceedings of the 2018 IEEE Symposium on VLSI Circuits, Honolulu, HI, USA, 18–22 June 2018*; IEEE: New York, NY, USA, 2018.
11. Cao, Y.; Xing, G.; Lin, H.; Zhang, N.; Zheng, H.; Wang, K. Prospect of Spin-Orbitronic Devices and Their Applications. *iScience* **2020**, *23*, 101614. [CrossRef] [PubMed]
12. Han, X.; Wang, X.; Wan, C.; Yu, G.; Lv, X. Spin-Orbit Torques: Materials, Physics, and Devices. *Appl. Phys. Lett.* **2021**, *118*, 120502. [CrossRef]
13. Nguyen, V.D.; Rao, S.; Wostyn, K.; Couet, S. Recent Progress in Spin-Orbit Torque Magnetic Random-Access Memory. *npj Spintron.* **2024**, *2*, 48. [CrossRef]
14. Ikeda, S.; Miura, K.; Yamamoto, H.; Mizunuma, K.; Gan, H.D.; Endo, M.; Kanai, S.; Hayakawa, J.; Matsukura, F.; Ohno, H. A Perpendicular-Anisotropy CoFeB–MgO Magnetic Tunnel Junction. *Nat. Mater.* **2010**, *9*, 721–724. [CrossRef] [PubMed]
15. Miron, I.M.; Garello, K.; Gaudin, G.; Zermatten, P.J.; Costache, M.V.; Auffret, S.; Bandiera, S.; Rodmacq, B.; Schuhl, A.; Gambardella, P. Perpendicular Switching of a Single Ferromagnetic Layer induced by in-plane Current Injection. *Nature* **2011**, *476*, 189–193. [CrossRef] [PubMed]
16. Lee, K.S.; Lee, S.W.; Min, B.C.; Lee, K.J. Threshold Current for Switching of a Perpendicular Magnetic Layer induced by Spin Hall Effect. *Appl. Phys. Lett.* **2013**, *102*, 112410. [CrossRef]
17. Zhang, X.; Xu, Z.; Zhu, Z. Revisiting the Analytical Solution of Spin-Orbit Torque Switched Nanoscale Perpendicular Ferromagnets. *Phys. Rev. B* **2024**, *110*, 184428. [CrossRef]
18. Taniguchi, T.; Mitani, S.; Hayashi, M. Critical Current Destabilizing Perpendicular Magnetization by the Spin Hall Effect. *Phys. Rev. B* **2015**, *92*, 024428. [CrossRef]
19. Park, E.S.; Lee, D.K.; Xue, F.; Min, B.C.; Koo, H.C.; Haney, P.M.; Kim, K.W.; Lee, K.J. Strong higher-order Angular Dependence of Spin-Orbit Torque in W/CoFeB Bilayer. *Phys. Rev. B* **2023**, *107*, 064411. [CrossRef]
20. Jørstad, N.P.; Pruckner, B.; Goes, W.; Selberherr, S.; Sverdlov, V. Spin Currents and Torques in Ferromagnetic Systems with Strong Interfacial Spin-Orbit Coupling. *Sci. Rep.* **2025**, *15*, 38749. [CrossRef] [PubMed]
21. Devda, H.; Deák, A.; Salemi, L.; Rózsa, L.; Szunyogh, L.; Oppeneer, P.M.; Nowak, U. Anatomy of Spin-Orbit-Torque-Assisted Magnetization Dynamics in Co/Pt Bilayers: Importance of the Orbital Torque. *Phys. Rev. B* **2025**, *112*, 144438. [CrossRef]
22. Dove, D.B. Demagnetizing Fields in Thin Magnetic Films. *Bell Syst. Tech. J.* **1967**, *46*, 1527–1559. [CrossRef]
23. Pruckner, B.; Sverdlov, V.; Selberherr, S. Optimal Current Regime for Reliable Switching of Perpendicular SOT-MRAM. In Proceedings of the 2026 European Symposium on Reliability of Electron Devices, Failure Physics and Analysis (ESREF), Vienna, Austria, 21–24 September 2026.
24. Hadámek, T.; Jørstad, N.P.; de Orio, R.L.; Goes, W.; Selberherr, S.; Sverdlov, V. A Comprehensive Study of Temperature and Its Effects in SOT-MRAM Devices. *Micromachines* **2023**, *14*, 1581. [CrossRef] [PubMed]
25. Zhang, C.; Fukami, S.; Sato, H.; Matsukura, F.; Ohno, H. Spin-Orbit Torque induced Magnetization Switching in Nano-Scale Ta/CoFeB/MgO. *Appl. Phys. Lett.* **2015**, *107*, 012401. [CrossRef]
26. Fukami, S.; Ohno, H. Magnetization Switching Schemes for Nanoscale Three-Terminal Spintronics Devices. *Jpn. J. Appl. Phys.* **2017**, *56*, 0802A1. [CrossRef]
27. Garello, K.; Miron, I.M.; Avci, C.O.; Freimuth, F.; Mokrousov, Y.; Blügel, S.; Auffret, S.; Boulle, O.; Gaudin, G.; Gambardella, P. Symmetry and Magnitude of Spin–Orbit Torques in Ferromagnetic Heterostructures. *Nat. Nanotechnol.* **2013**, *8*, 587–593. [CrossRef] [PubMed]
28. Krizakova, V.; Hoffmann, M.; Kateel, V.; Rao, S.; Couet, S.; Kar, G.S.; Garello, K.; Gambardella, P. Tailoring the Switching Efficiency of Magnetic Tunnel Junctions by the Fieldlike Spin-Orbit Torque. *Phys. Rev. Appl.* **2022**, *18*, 044070. [CrossRef]
29. Ray, K.; Vigier, J.; Usé, P.; Martin, S.; Lefoulon, N.; Bouard, C.; Drouard, M.; Gaudin, G. Intrinsic Back-Switching Phenomenon in Spin-Orbit Torque MRAM Devices. *Phys. Rev. Appl.* **2025**, *24*, 064038. [CrossRef]
30. Igarashi, Y.; Fujimoto, J. Modeling Ballistic Magnetization Reversals via Spin-Orbit Torques by Reinforcement Learning. *Phys. Rev. B* **2026**, *113*, 104428. [CrossRef]
31. Xu, Y.; Wang, C.; Shi, Y.; Cao, X.; Li, Z.; Zeng, D.; Ji, Z.; Gu, Y.; Wang, M.; Chen, Y.; et al. Investigation of Backward Sswitching and Write Margin Optimization of SOT-MTJ Devices. *Appl. Phys. Lett.* **2026**, *128*, 122405. [CrossRef]
32. Mikuszeit, N.; Boulle, O.; Miron, I.M.; Garello, K.; Gambardella, P.; Gaudin, G.; Buda-Prejbeanu, L.D. Spin-Orbit Torque driven Chiral Magnetization Reversal in Ultrathin Nanostructures. *Phys. Rev. B* **2015**, *92*, 144424. [CrossRef]

Disclaimer/Publisher's Note: The statements, opinions and data contained in all publications are solely those of the individual author(s) and contributor(s) and not of MDPI and/or the editor(s). MDPI and/or the editor(s) disclaim responsibility for any injury to people or property resulting from any ideas, methods, instructions or products referred to in the content.